

## VIP Electrocatalysis Very Important Paper

How to cite:

International Edition: doi.org/10.1002/anie.202103398

German Edition: doi.org/10.1002/ange.202103398

Tricycloquinazoline-Based 2D Conductive Metal–Organic Frameworks as Promising Electrocatalysts for CO<sub>2</sub> ReductionJingjuan Liu<sup>+</sup>, Dan Yang<sup>+</sup>, Yi Zhou<sup>+</sup>, Guang Zhang, Guolong Xing, Yunpeng Liu, Yanhang Ma,<sup>\*</sup> Osamu Terasaki, Shubin Yang,<sup>\*</sup> and Long Chen<sup>\*</sup>

**Abstract:** 2D conductive metal–organic frameworks (2D c-MOFs) are promising candidates for efficient electrocatalysts for the CO<sub>2</sub> reduction reaction (CO<sub>2</sub>RR). A nitrogen-rich tricycloquinazoline (TQ) based multitopic catechol ligand was used to coordinate with transition-metal ions (Cu<sup>2+</sup> and Ni<sup>2+</sup>), which formed 2D graphene-like porous sheets: M<sub>3</sub>(HHTQ)<sub>2</sub> (M = Cu, Ni; HHTQ = 2,3,7,8,12,13-Hexahydroxytricycloquinazoline). M<sub>3</sub>(HHTQ)<sub>2</sub> can be regarded as a single-atom catalyst where Cu or Ni centers are uniformly distributed in the hexagonal lattices. Cu<sub>3</sub>(HHTQ)<sub>2</sub> exhibited superior catalytic activity towards CO<sub>2</sub>RR in which CH<sub>3</sub>OH is the sole product. The Faradic efficiency of CH<sub>3</sub>OH reached up to 53.6% at a small over-potential of −0.4 V. Cu<sub>3</sub>(HHTQ)<sub>2</sub> exhibited larger CO<sub>2</sub> adsorption energies and higher activities over the isostructural Ni<sub>3</sub>(HHTQ)<sub>2</sub> and the reported archetypical Cu<sub>3</sub>-(HHTP)<sub>2</sub>. There is a strong dependence of both metal centers and the N-rich ligands on the electrocatalytic performance.

## Introduction

Overwhelmingly combusting fossil fuels has triggered horrible environmental problems, for example, global warming which is severely impairing the ecosystem, mainly due to excessive CO<sub>2</sub> emission.<sup>[1]</sup> As such, great efforts have been devoted to dispose and utilize CO<sub>2</sub> in recent years.<sup>[2]</sup> In particular, converting CO<sub>2</sub> into valuable chemicals driven by electricity represents a viable strategy to accelerate carbon recycling and alleviate the environmental problems.<sup>[3]</sup> To date,

many research works have been documented focusing on the electrochemical reduction of CO<sub>2</sub> into CO as the product because of the efficient and simple reaction pathway. Nevertheless, transforming CO<sub>2</sub> into other value-added chemicals or fuels, such as methane, ethane, methanol, and ethanol, is thermodynamically sluggish due to the chemical passivation of CO<sub>2</sub> with a low standard molar Gibbs free energy of formation (−394.4 kJ mol<sup>−1</sup>).<sup>[4]</sup> Therefore, how to effectively activate inert CO<sub>2</sub> molecule is a critical scientific issue. In addition, compared with the two-electron involved process for producing CO, converting CO<sub>2</sub> into other C1 or C2 products usually involves multiple electron transfer.<sup>[5]</sup> For example, electrochemically reducing CO<sub>2</sub> into CH<sub>3</sub>OH requires six-electron and six-proton transfer process: CO<sub>2</sub> + 6H<sup>+</sup> + 6e<sup>−</sup> → CH<sub>3</sub>OH + H<sub>2</sub>O or CO<sub>2</sub> + 5H<sub>2</sub>O + 6e<sup>−</sup> → CH<sub>3</sub>OH + 6OH<sup>−</sup>, which bears an endothermic process, and consequently features high overpotential, poor selectivity, and low efficiency.<sup>[4]</sup> In this context, developing efficient electrocatalysts capable of converting CO<sub>2</sub> into other valuable liquid chemicals with high selectivity remains challenging.

Thus far, various heterogeneous catalysts, including metals,<sup>[6]</sup> metal oxides,<sup>[7]</sup> and graphene-based materials,<sup>[8]</sup> have been applied for CO<sub>2</sub>RR to obtain value-added chemicals with high electrocatalytic activity. For large-scale and practical applications, cost-effective transition metal based electrocatalysts have been extensively investigated for CO<sub>2</sub>RR, among which Cu-based ones show promising catalytic performance.<sup>[9]</sup> However, the large over-potentials significantly hinder their widespread applications. Furthermore, preventing metal-cluster aggregation and accurately controlling metal-particle sizes are challenging and are prerequisite to achieve highly efficient CO<sub>2</sub>RR. A range of strategies have been developed to boost the catalytic efficiency by immobilizing metal atoms on the surface, pores, or skeleton of porous materials, for example, MOFs and covalent organic frameworks (COFs) to mediate single-atom catalysts.<sup>[10]</sup> In particular, dispersing active metal ions uniformly on the skeletons of two-dimensional (2D) MOFs represents a promising strategy to render superior CO<sub>2</sub>RR performance.

As a burgeoning subclass of 2D materials, 2D c-MOFs are constructed by self-assembling transition metallic nodes with conjugated organic ligands containing multitopic *ortho*-substituted functional groups (−NH<sub>2</sub>, −OH, −SH, or −SeH).<sup>[11]</sup> Thanks to the strong in-plane d-π conjugations and compact out-of-plane π-π interactions, the 2D lattices are orderly arranged to form layer-stacked periodic frameworks with regular open channels, inherent porosities, high charge-

[\*] J. Liu,<sup>[‡]</sup> Dr. G. Zhang, Dr. G. Xing, Prof. L. Chen  
Department of Chemistry, Tianjin Key Laboratory of Molecular  
Optoelectronic Science, Tianjin University  
Tianjin 300072 (China)  
E-mail: long.chen@tju.edu.cn

D. Yang,<sup>[‡]</sup> Prof. S. Yang  
School of Materials Science and Engineering, Beihang University  
Beijing 100191 (China)  
E-mail: yangshubin@buaa.edu.cn

Y. Zhou,<sup>[‡]</sup> Prof. Y. Ma, Prof. O. Terasaki  
School of Physical Science and Technology, ShanghaiTech University  
Shanghai 201210 (China)  
E-mail: mayh2@shanghaitech.edu.cn

Dr. Y. Liu  
Institute of High Energy Physics, Chinese Academy of Sciences  
Beijing 100049 (China)

[‡] These authors contributed equally to this work.

Supporting information and the ORCID identification number(s) for the author(s) of this article can be found under:  
https://doi.org/10.1002/anie.202103398.

carrier mobilities, exciting electrical conductivities, and tuneable catalytic/redox active sites.<sup>[12]</sup> These merits make 2D *c*-MOFs advantageous for electrocatalytic reduction of CO<sub>2</sub>.<sup>[13]</sup> Although several reports have successfully reduced CO<sub>2</sub> into CO using conductive MOFs as electrocatalysts,<sup>[14]</sup> 2D *c*-MOF-mediated CO<sub>2</sub>-to-methanol transformation remains challenging due to the complex electron-transfer pathways and high energy barriers. To develop high-performance 2D *c*-MOF-based electrocatalysts, both ligand engineering and judicious selection of metals should be considered.

Herein, the nitrogen-rich and electron-deficient tricyclo-quinazoline (TQ) moiety was selected to integrate into the 2D MOF skeleton for facilitating CO<sub>2</sub> capture and catalysis.<sup>[15]</sup> Accordingly, a C<sub>3</sub>-symmetric 2,3,7,8,12,13-hexahydroxytricyclo-quinazoline (HHTQ)<sup>[16]</sup> was synthesized to coordinate with Ni<sup>2+</sup> and Cu<sup>2+</sup> respectively in square-planar geometry, resulting in nicely honeycomb-like networks with uniform hexagonal pores (Figure 1a). The resulted 2D MOFs, that is, M<sub>3</sub>(HHTQ)<sub>2</sub> (M = Cu or Ni) feature high metal contents of nearly 20 % (wt) with metal ions regularly anchored and distributed in the lattices, which suggests their potential as single-atom catalysts. To our delight, Cu<sub>3</sub>(HHTQ)<sub>2</sub> exhibits prominent activity toward electrochemical reduction of CO<sub>2</sub> into methanol with high selectivity (up to 53.6 %), decent efficiency and good durability. In sharp contrast, the isostructural Ni<sub>3</sub>(HHTQ)<sub>2</sub> and the well-known archetypical Cu<sub>3</sub>-(HHTP)<sub>2</sub><sup>[17]</sup> showcased much worse CO<sub>2</sub>RR performance. The reason for the big performance variation and underlined mechanism were further unraveled by systematic measurements and computational studies. This work provides new

insights into designing novel 2D *c*-MOFs as promising electrocatalysts for CO<sub>2</sub>RR through modulating the interplay of both the ligands and metal centers properly.

## Results and Discussion

A solvothermal reaction between HHTQ and hydrated Cu(NO<sub>3</sub>)<sub>2</sub> or Ni(OAc)<sub>2</sub> in a mixture of water and DMF afforded crystalline M<sub>3</sub>(HHTQ)<sub>2</sub> (Figure 1a). Scanning electron microscopy (SEM) reveals Cu<sub>3</sub>(HHTQ)<sub>2</sub> consists of rod-like microcrystals (length: 1–10 μm), while Ni<sub>3</sub>(HHTQ)<sub>2</sub> appears as polycrystalline without a well-defined morphology (Figure S1). The crystallographic information of M<sub>3</sub>(HHTQ)<sub>2</sub> was resolved through Pawley refinement of powder X-ray diffraction (PXRD), three-dimensional electron diffraction tomography (3D-EDT), high-resolution transmission electron microscopy (HRTEM), and selected-area electron diffraction (SAED) methods. It can be inferred that both M<sub>3</sub>(HHTQ)<sub>2</sub> are isostructural with little differences in unit cell parameters, as revealed by the similarity of their PXRD patterns and similar ionic size between Ni<sup>2+</sup> and Cu<sup>2+</sup>. The reconstructed 3D reciprocal lattice by 3D-EDT indicates the unit cell parameters of Cu<sub>3</sub>(HHTQ)<sub>2</sub> are *a* = *b* = 26.10 Å, *c* = 3.34 Å, and  $\alpha = \beta = 90^\circ$ ,  $\gamma = 120^\circ$  (Figure 1h and Figure S2), which are further refined to be *a* = *b* = 25.30 Å, *c* = 3.23 Å, and  $\alpha = \beta = 90^\circ$ ,  $\gamma = 120^\circ$  (Figure 1b) through Pawley refinement against experimental PXRD pattern. The coordination between Ni<sup>2+</sup>/Cu<sup>2+</sup> and the triangular HHTQ ligands may form honeycomb-like 2D nets with pore size of around 2.3 nm

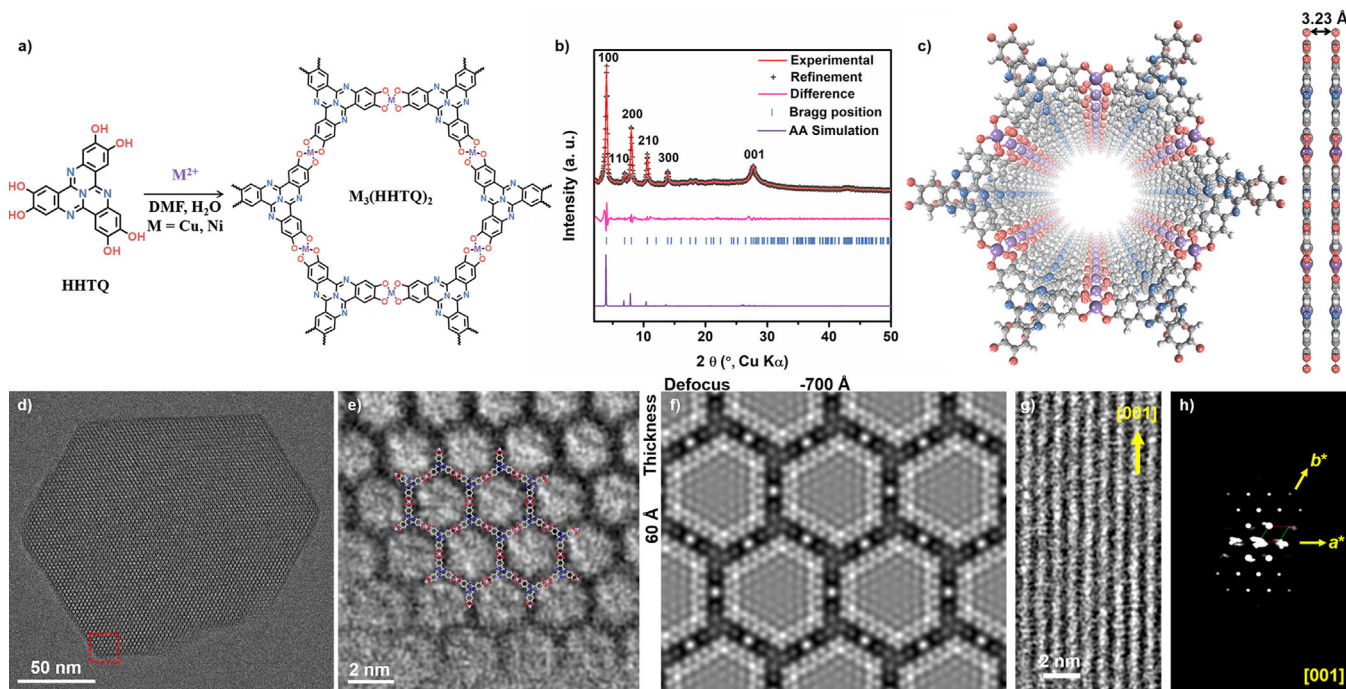


**Figure 1.** a) Synthesis of M<sub>3</sub>(HHTQ)<sub>2</sub> (M = Cu, Ni). b) Experimental and Pawley refined PXRD patterns of Cu<sub>3</sub>(HHTQ)<sub>2</sub>. c) A structural model of Cu<sub>3</sub>(HHTQ)<sub>2</sub>. C gray, N blue, O red, Cu purple, H white spheres. d) HRTEM image of Cu<sub>3</sub>(HHTQ)<sub>2</sub> taken along the *c* axis. e) Zoom-in view of HRTEM image for Cu<sub>3</sub>(HHTQ)<sub>2</sub> taken along the *c* axis that shows a hexagonal pore and ligand termination, overlaid with a structure model. f) Simulated TEM image along [001] direction. g) HRTEM image along [120] direction. h) Projection view of 3D EDT data of Cu<sub>3</sub>(HHTQ)<sub>2</sub> along [001] direction.



using different space groups ( $P6/m$  or  $P\bar{6}2m$ ), where the main difference is the alignment of N atoms in two linkers that connected to the same metal (Figure 1c; Supporting Information, Figure S3). However, these two possibilities are hard to be distinguished, so the one with higher symmetry  $P\bar{6}2m$  is adopted for illustration and calculation in this work.

Moreover, HRTEM images and SAED patterns along [001] direction show a honeycomb-like pore arrangement throughout the whole nanocrystal with  $d_{100} = d_{010} = 21.90$  Å, which is consistent with the crystal structure and simulation (Figure 1d–f; Supporting Information, Figure S4). It is noted that the crystal morphology also suggests the possibility for orthorhombic symmetry with the same structure. Although the EM observation of MOF materials remains challenging due to the severe beam-sensitivity,<sup>[18]</sup> the good crystallinity and conductivity enable the clear observation of crystal edge with ligands as termination (Figure 1e; Supporting Information, Figure S5). SAED patterns and HRTEM images of  $\text{Cu}_3(\text{HHTQ})_2$  nanocrystals perpendicular to  $c$  axis reveal an AA packing with an interlayer spacing of 3.3 Å (Figure 1h; Supporting Information, Figures S6, S7). Especially, the distance between adjacent layers corresponding to  $d_{001} = 3.3$  Å can be observed in the HRTEM image along the  $[120]$  zone axis (Figure 1g). Considering all of these,  $\text{Cu}_3(\text{HHTQ})_2$  are resolved to be honeycomb-like 2D networks which are further stacked along the  $c$  axis by  $\pi$ - $\pi$  interactions and thereby affording regular and open 1D hexagonal channels along the [001] direction. To further unravel the valency states of coordinated metal ions and their atomic neighboring structure, the X-ray absorption fine-structure (XAFS) spectra were collected at the Cu/Ni K edges (Figure 2a,b; Supporting Information, Figure S9).  $\text{Cu}_3(\text{HHTQ})_2$  displays almost the same white-line peak as that of CuO, which suggests Cu ions exhibit +2 oxidation state in  $\text{Cu}_3(\text{HHTQ})_2$ . Similarly, Ni ions in  $\text{Ni}_3(\text{HHTQ})_2$  feature the same oxidation

state as that of NiO (+2). In addition, Fourier transform (FT) spectra of extended X-ray absorption fine structure (EXAFS) oscillation  $k^3\chi(k)$  for  $\text{M}_3(\text{HHTQ})_2$  and their corresponding fitting parameters are also given in the Supporting Information, Figures S10, S11 and Tables S1, S2. The first coordination peak of  $\text{Cu}_3(\text{HHTQ})_2$  corresponds to the Cu–O bond with a distance of 1.93 Å (2.05 Å for Ni–O) and the second coordination peak is attributed to Cu–C interaction with a distance of 2.67 Å (2.69 Å for Ni–C). Inspiringly, metallic Cu or Ni are absent in these complexes. Therefore, the XAFS spectra provide strong evidence on the formation of  $\text{MO}_4$  complexes in these  $\text{M}_3(\text{HHTQ})_2$ .

The chemical compositions of  $\text{M}_3(\text{HHTQ})_2$  were surveyed by Fourier-transform infrared spectroscopy (FTIR; Supporting Information, Figure S12). The significant attenuation of O–H stretching vibration above  $3000\text{ cm}^{-1}$  suggests successful coordination between metal ions and catechol ligands. Besides, the characteristic peaks of TQ moiety locate at around 1641, 1594, 1316, and  $1262\text{ cm}^{-1}$ . XPS spectra of  $\text{Cu}_3(\text{HHTQ})_2$  and  $\text{Ni}_3(\text{HHTQ})_2$  (Supporting Information, Figures S13, S14) disclose the signals of C 1s, N 1s, O 1s, and M (Cu and Ni) 2p. Inspecting high-resolution regions of M (2p) and O (1s) indicates the formation of square-planar metal bis(dihydroxy) complexes. The peak of Cu 2p  $2/3$  at 934.5 eV reveals the +2 state of Cu. The bands of O 1s for  $\text{Cu}_3(\text{HHTQ})_2$  at 531.13 and 532.76 eV are assignable to oxygens from ligand and  $\text{CuO}_4$  segments, respectively (530.52 and 532.04 eV for  $\text{Ni}_3(\text{HHTQ})_2$ ). The high-resolution N 1s and C 1s spectra manifest the existence of TQ core. Electron paramagnetic resonance (EPR) spectrum of  $\text{Cu}_3(\text{HHTQ})_2$  shows a strong signal at  $g = 2.07$  which corresponds to the characteristic metal-centered radicals, while no radical is detected in  $\text{Ni}_3(\text{HHTQ})_2$  (Supporting Information, Figure S15). The porosities of  $\text{M}_3(\text{HHTQ})_2$  were assessed by  $\text{N}_2$  adsorption/desorption isotherms at 77 K, which reveal the Brunauer–Emmett–Teller (BET) surface areas of  $\text{Cu}_3(\text{HHTQ})_2$  and  $\text{Ni}_3(\text{HHTQ})_2$  are 104 and  $311\text{ m}^2\text{ g}^{-1}$ , respectively (Supporting Information, Figure S16). Thermogravimetric analysis (TGA) suggests both  $\text{Cu}_3(\text{HHTQ})_2$  and  $\text{Ni}_3(\text{HHTQ})_2$  display pronounced weight losses above  $200^\circ\text{C}$ , probably due to the structure decomposition (Supporting Information, Figure S17).

Interestingly, solid-state diffuse reflectance UV-vis-NIR spectra of  $\text{Cu}_3(\text{HHTQ})_2$  and  $\text{Ni}_3(\text{HHTQ})_2$  powders show broad absorption extending to the NIR region, corresponding to small band gaps of around 1.33 and 1.15 eV respectively owing to the strong  $\pi$ -d (in-plane) and  $\pi$ - $\pi$  (out-of-plane) conjugations for both MOFs (Supporting Information, Figure S18). We further evaluated electrical conductivities of both MOFs in bulk samples with two-probe method. The conductivities of  $\text{Cu}_3(\text{HHTQ})_2$  and  $\text{Ni}_3(\text{HHTQ})_2$  are about  $2.74 \pm 0.15 \times 10^{-5}\text{ S cm}^{-1}$  and  $2.27 \pm 0.19 \times 10^{-4}\text{ S cm}^{-1}$ , respectively under ambient conditions, which show negligible change regardless of the pellet thickness (Supporting Information, Figure S19). Noteworthy, a very interesting anisotropic transport behavior was just recently demonstrated by Dincă and co-workers based on the single-crystal conductivity measurements via four-probe method showing much higher conductivity beyond about  $10\text{ S cm}^{-1}$ .<sup>[19]</sup> Furthermore, the

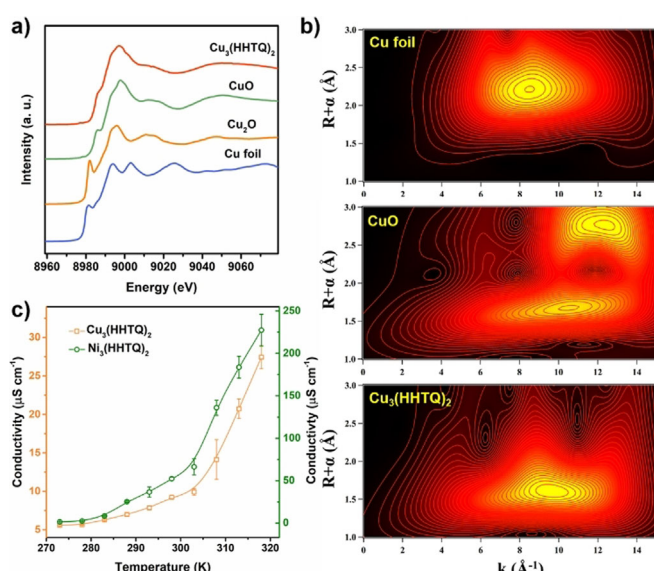


**Figure 2.** a) XANES spectra of Cu K-edge for the standard Cu foil,  $\text{Cu}_2\text{O}$ , CuO, and  $\text{Cu}_3(\text{HHTQ})_2$  sample. b) Wavelet transforms of  $\text{Cu}_3(\text{HHTQ})_2$  and the standard Cu foil and CuO samples. c) Temperature-dependent conductance of  $\text{Cu}_3(\text{HHTQ})_2$  and  $\text{Ni}_3(\text{HHTQ})_2$  pellets.



conductivities exhibit nonlinear enhancement with increasing temperature, which implies a semiconducting nature (Figure 2c). The decent conductivities of both 2D *c*-MOFs suggest their prospects in electrocatalysis.

To investigate the performance of  $M_3(\text{HHTQ})_2$  for electrocatalytic  $\text{CO}_2\text{RR}$ , we performed the initial tests for  $\text{Cu}_3(\text{HHTQ})_2$ ,  $\text{Ni}_3(\text{HHTQ})_2$  and  $\text{Cu}_3(\text{HHTP})_2$  in a three-electrode cell containing aqueous  $\text{KHCO}_3$  solution (0.1 M) as electrolyte and 2D *c*-MOF/acetylene black (2:1, wt) composite loaded on carbon fiber paper as the working electrode. The linear sweep voltammetry (LSV) curve for  $\text{Cu}_3(\text{HHTQ})_2$  in  $\text{CO}_2$ -saturated electrolyte exhibits higher current densities compared to that in Ar-saturated solution with a scan rate of  $5 \text{ mV s}^{-1}$  (Figure 3a). Besides, in  $\text{CO}_2$ -saturated electrolyte,  $\text{Cu}_3(\text{HHTQ})_2$  delivers the highest current densities compared to  $\text{Ni}_3(\text{HHTQ})_2$  and  $\text{Cu}_3(\text{HHTP})_2$ , with a current density of  $45 \text{ mA cm}^{-2}$  at  $-1.2 \text{ V}$  (vs. RHE) (Figure 3b). These results suggest the great potential of  $\text{Cu}_3(\text{HHTQ})_2$  as promising electrocatalyst for  $\text{CO}_2\text{RR}$ . Furthermore, the electrocatalytic  $\text{CO}_2\text{RR}$  process using  $\text{Cu}_3(\text{HHTQ})_2$ ,  $\text{Ni}_3(\text{HHTQ})_2$  and  $\text{Cu}_3(\text{HHTP})_2$  at different potentials (from  $-0.2$  to  $-0.8 \text{ V}$  vs. RHE) were investigated. The products were analyzed by gas chromatography (GC) and nuclear magnetic resonance (NMR) spectroscopy. Inspiringly, besides  $\text{H}_2$ ,  $\text{CH}_3\text{OH}$  is the

only detected product throughout the entire range of potentials. In addition, the  $\text{CO}_2\text{RR}$  performance is strongly dependent on the type of metal centers, organic linkers, and the applied potentials. As shown in Figure 3c,  $\text{Cu}_3(\text{HHTQ})_2$  catalyst showcases the best  $\text{CO}_2\text{RR}$  performance among the others and delivers the highest Faradic efficiency toward  $\text{CH}_3\text{OH}$  ( $\text{FE}_{\text{CH}_3\text{OH}}$ ) of 53.6% at  $-0.4 \text{ V}$  vs. RHE, which is about 100 times larger than those of  $\text{Ni}_3(\text{HHTQ})_2$  and  $\text{Cu}_3(\text{HHTP})_2$  with only 0.54% and 0.15%, respectively. Besides,  $\text{Ni}_3(\text{HHTQ})_2$  and  $\text{Cu}_3(\text{HHTP})_2$  render the best  $\text{FE}_{\text{CH}_3\text{OH}}$  of 5.4% and 1.9% respectively at  $-0.3 \text{ V}$  vs. RHE (Supporting Information, Figures S22, S23). Tafel slopes were further used to evaluate the kinetics of  $\text{CO}_2\text{RR}$  catalyzed by these 2D *c*-MOFs.  $\text{Cu}_3(\text{HHTQ})_2$  showcased the lowest Tafel slope of  $285.87 \text{ mV dec}^{-1}$  toward  $\text{CH}_3\text{OH}$  production compared to that of  $\text{Ni}_3(\text{HHTQ})_2$  ( $310.05 \text{ mV dec}^{-1}$ ) and  $\text{Cu}_3(\text{HHTP})_2$  ( $305.7 \text{ mV dec}^{-1}$ ) (Supporting Information, Figure S24), further confirming its faster kinetics. Additionally, the TON of  $\text{Cu}_3(\text{HHTQ})_2$ ,  $\text{Ni}_3(\text{HHTQ})_2$  and  $\text{Cu}_3(\text{HHTP})_2$  are calculated as 353, 30, and 38, respectively. Besides,  $\text{Cu}_3(\text{HHTQ})_2$  demonstrates the lowest overpotential of  $-0.4 \text{ V}$ , which indicates its excellent energy efficiency for the electrochemical conversion of  $\text{CO}_2$  and is superior to most Cu- and MOFs-based electrocatalysts (see the Supporting Information, Table S4 for a detailed comparison). The catalytic durability of  $\text{Cu}_3(\text{HHTQ})_2$  was evaluated by long-term electrolysis process and the results indicated that a stable  $\text{CO}_2\text{RR}$  performance of  $\text{Cu}_3(\text{HHTQ})_2$  was maintained without notable degeneration for at least ten hours at  $-0.4 \text{ V}$  vs. RHE (Figure 3e).

To understand the obvious difference on the catalytic performance between  $\text{Cu}_3(\text{HHTQ})_2$  and the isostructural  $\text{Ni}_3(\text{HHTQ})_2$  as well as the archetypical analogue of  $\text{Cu}_3(\text{HHTP})_2$ ,<sup>[17]</sup> the  $\text{CO}_2$  and proton adsorption capabilities of  $\text{MO}_4$  sites in these three 2D *c*-MOFs were estimated through density functional theory (DFT) calculations. As depicted in Figure 4b,  $\text{Cu}_3(\text{HHTQ})_2$  displayed the strongest  $\text{CO}_2$  adsorp-

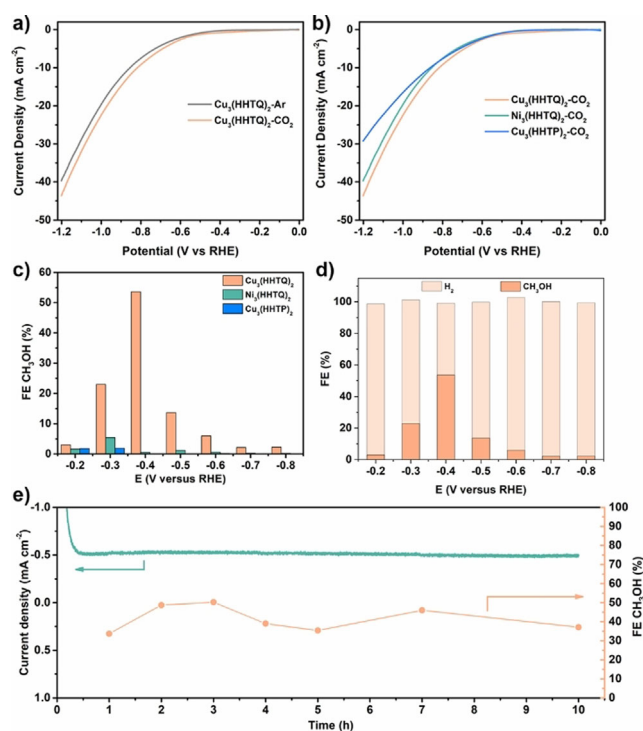


**Figure 3.**  $\text{CO}_2\text{RR}$  performance of  $\text{Cu}_3(\text{HHTQ})_2$ ,  $\text{Ni}_3(\text{HHTQ})_2$ ,  $\text{Cu}_3(\text{HHTP})_2$  in 0.1 M  $\text{KHCO}_3$ . a) LSV curves for  $\text{Cu}_3(\text{HHTQ})_2$  in Ar- (grey line) or  $\text{CO}_2$ - (orange line) saturated 0.1 M  $\text{KHCO}_3$  electrolyte with a scan rate of  $5 \text{ mV s}^{-1}$ . b) LSV curves of  $\text{Cu}_3(\text{HHTQ})_2$ ,  $\text{Ni}_3(\text{HHTQ})_2$ ,  $\text{Cu}_3(\text{HHTP})_2$  in  $\text{CO}_2$ -saturated 0.1 M  $\text{KHCO}_3$  electrolyte with a scan rate of  $5 \text{ mV s}^{-1}$ . c)  $\text{CH}_3\text{OH}$  FEs for  $\text{Cu}_3(\text{HHTQ})_2$ ,  $\text{Ni}_3(\text{HHTQ})_2$ ,  $\text{Cu}_3(\text{HHTP})_2$  at different potentials. d) The selectivity for each product ( $\text{CH}_3\text{OH}$  and  $\text{H}_2$ ) for  $\text{Cu}_3(\text{HHTQ})_2$  at different potentials. (e) Chronoamperometric measurements and  $\text{CH}_3\text{OH}$  FEs for  $\text{Cu}_3(\text{HHTQ})_2$  at  $-0.4 \text{ V}$  vs. RHE with 10-hour tests.

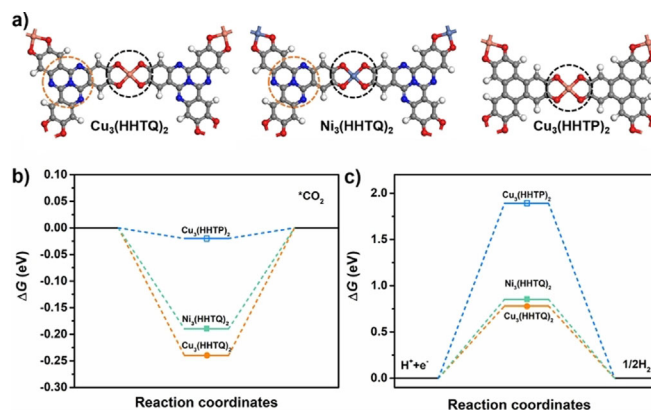


**Figure 4.** a) Atomistic structure of  $\text{Cu}_3(\text{HHTQ})_2$ ,  $\text{Ni}_3(\text{HHTQ})_2$ , and  $\text{Cu}_3(\text{HHTP})_2$ . C gray, N blue, O red, H white, Cu orange, Ni lavender. The dark dashed circles indicate the catalytic active sites with  $\text{MO}_4$  units. The orange dashed circles indicate the nitrogen-rich organic cores. b) Free-energy profiles of  $\text{CO}_2$  on  $\text{MO}_4$  units in the  $\text{Cu}_3(\text{HHTQ})_2$ ,  $\text{Ni}_3(\text{HHTQ})_2$ ,  $\text{Cu}_3(\text{HHTP})_2$ , respectively. c) Free-energy profiles of H on  $\text{MO}_4$  units of  $\text{Cu}_3(\text{HHTQ})_2$ ,  $\text{Ni}_3(\text{HHTQ})_2$ ,  $\text{Cu}_3(\text{HHTP})_2$ , respectively.



tion ability with Gibbs free energy ( $\Delta G$ ) of  $-0.24$  eV among the three MOFs, followed the order of  $\text{Ni}_3(\text{HHTQ})_2$  ( $\Delta G$ :  $-0.19$  eV) and lastly  $\text{Cu}_3(\text{HHTQ})_2$  ( $\Delta G$ :  $-0.02$  eV). Moreover, theoretical results suggest that it is not favorable to adsorb proton for all three MOFs (Figure 4c). Thus,  $\text{Cu}_3(\text{HHTQ})_2$  represents the best  $\text{CO}_2\text{RR}$  electrocatalyst among the three MOFs, which exhibits lowest HER energy barrier and fastest proton/electron transfer kinetics.

DFT calculations were further performed to provide insights into the mechanism of electrochemical production of  $\text{CH}_3\text{OH}$  catalyzed by  $\text{Cu}_3(\text{HHTQ})_2$ . A monolayer lattice of  $\text{Cu}_3(\text{HHTQ})_2$  was applied as the model to optimize the structures of the intermediates involved in the six-proton/six-electron ( $6\text{H}^+/6\text{e}^-$ ) transfer process toward electrochemical reduction of  $\text{CO}_2$  into  $\text{CH}_3\text{OH}$ . The Gibbs free energies diagrams for optimized configurations of intermediates at each step are summarized in Figure 5a, and the by-products are also taken into account. The optimized structures at each step with the lowest energy are shown in Figure 5b. Firstly, two possible reaction pathways are proposed for the first proton-electron ( $\text{H}^+/\text{e}^-$ ) pair transfer process. From an energy point of view, a  $\text{H}^+/\text{e}^-$  attacking the carbon atom of  $\text{CO}_2$  to form  $^*\text{OCHO}$  intermediate renders a relatively lower energy increase than that on oxygen atom to form  $^*\text{COOH}$  ( $0.70$  vs.  $0.72$  eV). This  $^*\text{CO}_2 \rightarrow ^*\text{OCHO}$  step is the potential determining step (PDS) during the  $\text{CO}_2\text{RR}$  process. Afterwards, the

second hydrogenation occurs at an oxygen atom to generate  $^*\text{HCOOH}$  with an energy release of  $0.88$  eV, rather than occurring at carbon atom to form  $^*\text{OCH}_2\text{O}$  involving  $1.32$  eV energy increase, which indicates converting  $^*\text{OCHO}$  into  $^*\text{HCOOH}$  intermediate on  $\text{Cu}_3(\text{HHTQ})_2$  is thermodynamically favorable. In the third step, hydrogenation occurs at an oxygen atom with eliminating a  $\text{H}_2\text{O}$  molecule and forming a  $^*\text{CHO}$  intermediate, which is accompanied by the free energy uphill with the value of  $0.67$  eV. In this step, generating  $^*\text{OCH}$  moiety seems unfavorable due to its higher energy injection than  $^*\text{CHO}$ . Subsequently, the fourth  $\text{H}^+/\text{e}^-$  pair reacts with  $^*\text{CHO}$  to afford  $^*\text{CH}_2\text{O}$  with a decreased energy of  $0.17$  eV. The other possible product of this step is  $^*\text{CHOH}$ , which however, bears a relatively high energy injection of  $1.09$  eV. Afterwards, the reaction between the fifth  $\text{H}^+/\text{e}^-$  and  $^*\text{CH}_2\text{O}$  produces  $^*\text{CH}_2\text{OH}$  with an energy reduction by  $0.56$  eV, in which the potential product of  $^*\text{CH}_3\text{O}$  seems not likely to dictate due to its obvious energy uphill of  $0.96$  eV. Next,  $^*\text{CH}_3\text{OH}$  is obtained with the reaction between the sixth  $\text{H}^+/\text{e}^-$  pair and  $^*\text{CH}_2\text{OH}$  with an energy release of  $0.33$  eV. The final step is the desorption of  $\text{CH}_3\text{OH}$  from  $\text{Cu}_3(\text{HHTQ})_2$  with an energy increase by  $0.21$  eV. Consequently, the most favorable reacting pathway for  $\text{Cu}_3(\text{HHTQ})_2$ -electrocatalyzed  $\text{CO}_2\text{RR}$  is shown as follows:  $\text{CO}_2(\text{g}) \rightarrow ^*\text{OCHO} \rightarrow ^*\text{HCOOH} \rightarrow ^*\text{CHO} \rightarrow ^*\text{CH}_2\text{O} \rightarrow ^*\text{CH}_2\text{OH} \rightarrow ^*\text{CH}_3\text{OH} \rightarrow ^* + \text{CH}_3\text{OH}$  (inset of Figure 5a). The correspond-

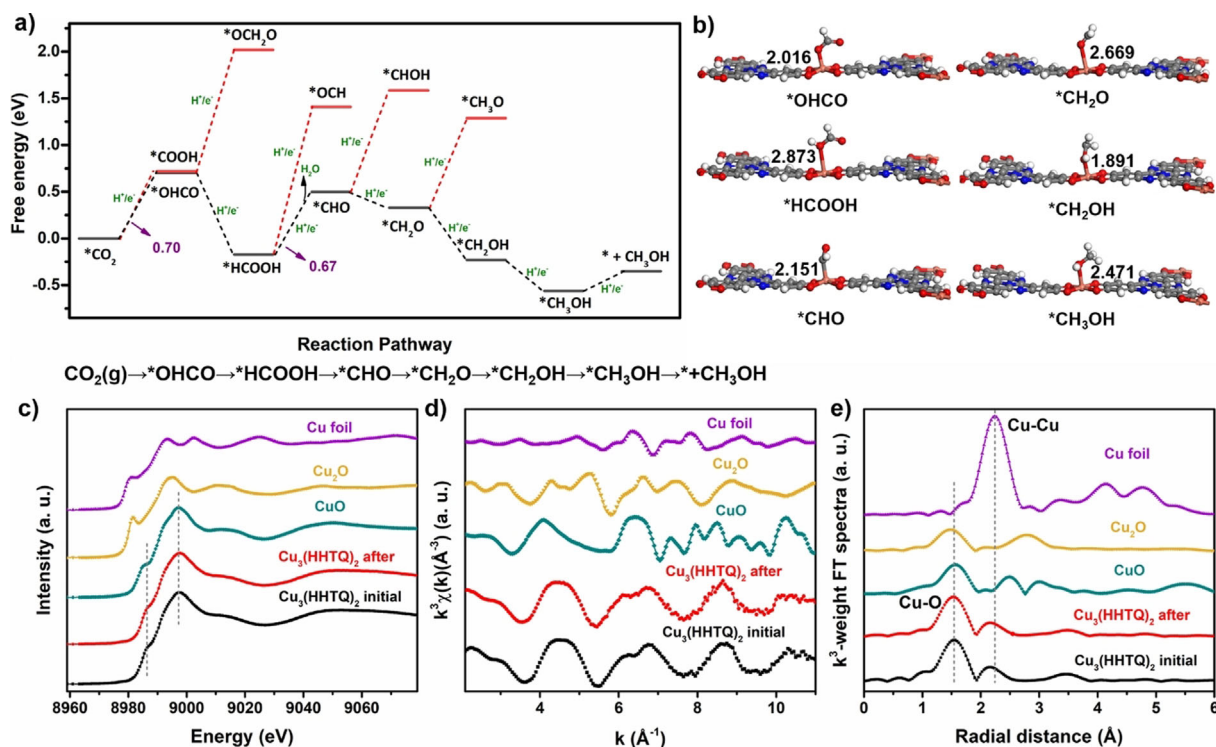


**Figure 5.** a) Free energy profiles for the  $\text{CO}_2\text{RR}$  on  $\text{Cu}_3(\text{HHTQ})_2$ . The proposed catalytic mechanism for electrochemical reduction of  $\text{CO}_2$  to  $\text{CH}_3\text{OH}$  by  $\text{Cu}_3(\text{HHTQ})_2$  is shown at the bottom. b) Structures of the catalyst and key reaction intermediates involved in the proposed reaction mechanism for the  $\text{CO}_2\text{RR}$  on  $\text{Cu}_3(\text{HHTQ})_2$ . The bond lengths and distances are labeled in Å. \* represent to chemisorbed species. c) Cu K-edge XANES spectra of Cu foil,  $\text{Cu}_2\text{O}$ ,  $\text{CuO}$ , and  $\text{Cu}_3(\text{HHTQ})_2$  samples before and after  $\text{CO}_2\text{RR}$ . d) Cu K-edge EXAFS oscillations  $k^3\chi(k)$  for Cu foil,  $\text{Cu}_2\text{O}$ ,  $\text{CuO}$ , and  $\text{Cu}_3(\text{HHTQ})_2$  before and after  $\text{CO}_2\text{RR}$ . e) Cu K-edge FT spectra of Cu foil,  $\text{Cu}_2\text{O}$ ,  $\text{CuO}$ , and  $\text{Cu}_3(\text{HHTQ})_2$  before and after  $\text{CO}_2\text{RR}$ .

ing calculations for  $\text{Ni}_3(\text{HHTQ})_2$  and  $\text{Cu}_3(\text{HHTQ})_2$  electrocatalysts are summarized as Section 15 in Supporting Information.

The structural stability of  $\text{Cu}_3(\text{HHTQ})_2$  after long-term testing was confirmed by the unchanged PXRD pattern, FT-IR and Raman spectra after  $\text{CO}_2\text{RR}$  (Supporting Information, Figures S30–S32). Besides, XPS spectrum  $\text{Cu}_3(\text{HHTQ})_2$  after catalysis was tested which further indicate the HHTQ ligand in the framework was stable during the  $\text{CO}_2\text{RR}$  (Supporting Information, Figure S33).<sup>[12f]</sup> Additionally, XAFS spectra disclose the oxidation state of  $\text{Cu}^{\text{II}}$  within  $\text{Cu}_3(\text{HHTQ})_2$  is maintained as well throughout the catalytic process without any detectable signals of  $\text{Cu}^0$  or  $\text{Cu}^{\text{I}}$  (Figure 5c). Furthermore, EXAFS indicates the first coordination peak with a distance of 1.93 Å assigned to the Cu–O bond is not shifted and maintain the initial intensity, which suggests no obvious changes in Cu coordination number and bond length of Cu–O for  $\text{Cu}_3(\text{HHTQ})_2$  during the catalytic process (Figure 5e). Furthermore, the absence of characteristic signals of Cu–Cu (2.24 Å) again excludes the generation of metallic copper. Consequently, the well-defined  $\text{CuO}_4$  catalytic sites showcase excellent stability during the  $\text{CO}_2\text{RR}$  process.

## Conclusion

We successfully developed tricycloquinazoline based 2D *c*-MOFs as efficient electrocatalysts for converting  $\text{CO}_2$  into  $\text{CH}_3\text{OH}$ . Both theoretical and experimental results indicate  $\text{Cu}_3(\text{HHTQ})_2$  with electron-deficient but nitrogen-rich TQ cores displays the best electrocatalytic  $\text{CO}_2\text{RR}$  performance.  $\text{Cu}_3(\text{HHTQ})_2$  as electrocatalyst for  $\text{CO}_2\text{RR}$  shows high selectivity toward  $\text{CH}_3\text{OH}$  with Faradic efficiency up to 53.6% at a low overpotential of  $-0.4$  V, and maintains good durability, which is comparable and even better than other Cu- and MOFs-based electrocatalysts. The rational mechanism of six-proton/six-electron transfer process for  $\text{Cu}_3(\text{HHTQ})_2$ -catalyzed  $\text{CO}_2$ -to- $\text{CH}_3\text{OH}$  conversion was further proposed. This work highlights the interplay of both metal centers and organic ligands of 2D *c*-MOFs exerts essential roles in tuning the catalytic activity and selectivity towards efficient electrochemical  $\text{CO}_2\text{RR}$ .

## Acknowledgements

This work was financially supported by the National Key Research and Development Program of China (2017YFA0207500), National Natural Science Foundation of China (51973153, 92045303). This is also supported by the center for high-resolution electron microscopy (ChEM), ShanghaiTech University (EM02161943).

## Conflict of interest

The authors declare no conflict of interest.

**Keywords:**  $\text{CO}_2\text{RR}$  · conductivity · electrocatalysis · metal–organic frameworks · methanol

- [1] T. R. Karl, K. E. Trenberth, *Science* **2003**, 302, 1719.
- [2] J. Artz, T. E. Müller, K. Thenert, J. Kleinekorte, R. Meys, A. Sternberg, A. Bardow, W. Leitner, *Chem. Rev.* **2018**, 118, 434–504.
- [3] Y. Y. Birdja, E. Pérez-Gallent, M. C. Figueiredo, A. J. Göttele, F. Calle-Vallejo, M. T. M. Koper, *Nat. Energy* **2019**, 4, 732–745.
- [4] F. N. Al-Rowaili, A. Jamal, M. S. Ba Shammakh, A. Rana, *ACS Sustainable Chem. Eng.* **2018**, 6, 15895–15914.
- [5] J. Qiao, Y. Liu, F. Hong, J. Zhang, *Chem. Soc. Rev.* **2014**, 43, 631–675.
- [6] N. Han, Y. Wang, H. Yang, J. Deng, J. Wu, Y. Li, Y. Li, *Nat. Commun.* **2018**, 9, 1320.
- [7] D. Gao, Y. Zhang, Z. Zhou, F. Cai, X. Zhao, W. Huang, Y. Li, J. Zhu, P. Liu, F. Yang, G. Wang, X. Bao, *J. Am. Chem. Soc.* **2017**, 139, 5652–5655.
- [8] J. Liu, Q. Ma, Z. Huang, G. Liu, H. Zhang, *Adv. Mater.* **2019**, 31, 1800696.
- [9] S. Nitopi, E. Bertheussen, S. B. Scott, X. Liu, A. K. Engstfeld, S. Hørch, B. Seger, I. E. L. Stephens, K. Chan, C. Hahn, J. K. Nørskov, T. F. Jaramillo, I. Chorkendorff, *Chem. Rev.* **2019**, 119, 7610–7672.
- [10] T. Sun, L. Xu, D. Wang, Y. Li, *Nano Res.* **2019**, 12, 2067–2080.
- [11] a) L. Sun, M. G. Campbell, M. Dincă, *Angew. Chem. Int. Ed.* **2016**, 55, 3566–3579; *Angew. Chem.* **2016**, 128, 3628–3642; b) M. Ko, L. Mendecki, K. A. Mirica, *Chem. Commun.* **2018**, 54, 7873–7891; c) J. Liu, X. Song, T. Zhang, S. Liu, H. Wen, L. Chen, *Angew. Chem. Int. Ed.* **2021**, 60, 5612–5624; *Angew. Chem.* **2021**, 133, 5672–5684.
- [12] a) J. Park, A. C. Hinckley, Z. Huang, D. Feng, A. A. Yakovenko, M. Lee, S. Chen, X. Zou, Z. Bao, *J. Am. Chem. Soc.* **2018**, 140, 14533–14537; b) R. Dong, P. Han, H. Arora, M. Ballabio, M. Karakus, Z. Zhang, C. Shekhar, P. Adler, P. S. Petkov, A. Erbe, S. C. B. Mannsfeld, C. Felser, T. Heine, M. Bonn, X. Feng, E. Cánovas, *Nat. Mater.* **2018**, 17, 1027–1032; c) R. W. Day, D. K. Bediako, M. Rezaee, L. R. Parent, G. Skorupskii, M. Q. Arguilla, C. H. Hendon, I. Stassen, N. C. Gianneschi, P. Kim, M. Dincă, *ACS Cent. Sci.* **2019**, 5, 1959–1964; d) D. Sheberla, L. Sun, M. A. Blood-Forsythe, S. Er, C. R. Wade, C. K. Brozek, A. Aspuru-Guzik, M. Dincă, *J. Am. Chem. Soc.* **2014**, 136, 8859–8862; e) Y. Cui, J. Yan, Z. Chen, W. Xing, C. Ye, X. Li, Y. Zou, Y. Sun, C. Liu, W. Xu, D. Zhu, *iScience* **2020**, 23, 100812; f) K. Wada, K. Sakaushi, S. Sasaki, H. Nishihara, *Angew. Chem. Int. Ed.* **2018**, 57, 8886–8890; *Angew. Chem.* **2018**, 130, 9024–9028.
- [13] a) Y. Tian, C. Zhu, L. Yan, J. Zhao, Z. Su, *J. Mater. Chem. A* **2019**, 7, 15341–15346; b) X. Mao, C. Tang, T. He, D. Wijethunge, C. Yan, Z. Zhu, A. Du, *Nanoscale* **2020**, 12, 6188–6194.
- [14] a) R. Matheu, E. Gutierrez-Puebla, M. Á. Monge, C. S. Diercks, J. Kang, M. S. Prévot, X. Pei, N. Hanikel, B. Zhang, P. Yang, O. M. Yaghi, *J. Am. Chem. Soc.* **2019**, 141, 17081–17085; b) H. Zhong, M. Ghorbani-Asl, K. H. Ly, J. Zhang, J. Ge, M. Wang, Z. Liao, D. Makarov, E. Zschech, E. Brunner, I. M. Weidinger, J. Zhang, A. V. Krashennnikov, S. Kaskel, R. Dong, X. Feng, *Nat. Commun.* **2020**, 11, 1409; c) Z. Meng, J. Luo, W. Li, K. A. Mirica, *J. Am. Chem. Soc.* **2020**, 142, 21656–21669.
- [15] O. Buyukcakir, R. Yuksel, Y. Jiang, S. H. Lee, W. K. Seong, X. Chen, R. S. Ruoff, *Angew. Chem. Int. Ed.* **2019**, 58, 872–876; *Angew. Chem.* **2019**, 131, 882–886.
- [16] S. Kumar, E. J. Wachtel, E. Keinan, *J. Org. Chem.* **1993**, 58, 3821–3827.
- [17] a) M. Hmadeh, Z. Lu, Z. Liu, F. Gándara, H. Furukawa, S. Wan, V. Augustyn, R. Chang, L. Liao, F. Zhou, E. Perre, V. Ozolins, K. Suenaga, X. Duan, B. Dunn, Y. Yamamoto, O. Terasaki, O. M. Yaghi, *Chem. Mater.* **2012**, 24, 3511–3513; b) X. Song, X. Wang,



- Y. Li, C. Zheng, B. Zhang, C. A. Di, F. Li, C. Jin, W. Mi, L. Chen, W. Hu, *Angew. Chem. Int. Ed.* **2020**, *59*, 1118–1123; *Angew. Chem.* **2020**, *132*, 1134–1139.
- [18] a) D. Zhang, Y. Zhu, L. Liu, X. Ying, C. E. Hsiung, R. Sougrat, K. Li, Y. Han, *Science* **2018**, *359*, 675–679; b) Y. Zhou, X. Xu, A. Carlsson, S. Lazar, Z. Pan, Y. Ma, O. Terasaki, H. Deng, *Chem. Mater.* **2020**, *32*, 4966–4972.
- [19] a) J.-H. Dou, M. Q. Arguilla, Y. Luo, J. Li, W. Zhang, L. Sun, J. L. Mancuso, L. Yang, T. Chen, L. R. Parent, G. Skorupskii, N. J. Libretto, C. Sun, M. C. Yang, P. V. Dip, E. J. Brignole, J. T. Miller, J. Kong, C. H. Hendon, J. Sun, M. Dincă, *Nat. Mater.* **2021**, *20*, 222–228; b) R. Dong, X. Feng, *Nat. Mater.* **2021**, *20*, 122–123.
- Manuscript received: March 9, 2021  
Version of record online: ■ ■ ■ ■ ■ ■ ■ ■ ■ ■
-

## Research Articles

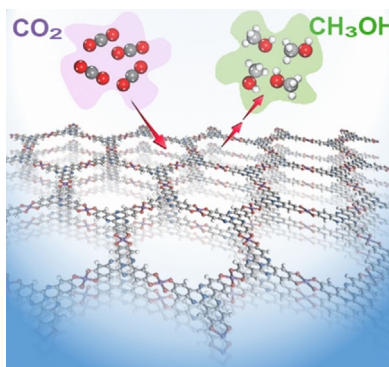
VIP

## Electrocatalysis



J. Liu, D. Yang, Y. Zhou, G. Zhang,  
G. Xing, Y. Liu, Y. Ma,\* O. Terasaki,  
S. Yang,\* L. Chen\* ——— ■■■—■■■

Tricycloquinazoline-Based 2D Conductive  
Metal–Organic Frameworks as Promising  
Electrocatalysts for CO<sub>2</sub> Reduction



Tricycloquinazoline (TQ) based 2D conductive MOFs were developed and employed as electrocatalysts for converting CO<sub>2</sub> into CH<sub>3</sub>OH. Cu<sub>3</sub>(HHTQ)<sub>2</sub> with electron-deficient but nitrogen-rich TQ cores displays the best electrocatalytic CO<sub>2</sub>RR performance, showing high selectivity toward CH<sub>3</sub>OH with Faradic efficiency up to 53.6% at a low overpotential of −0.4 V and maintained good durability.